

FRACTURE AND GRAIN BOUNDARY DAMAGE IN AM NI-BASED SUPERALLOYS UNDER HIGH-TEMPERATURE TENSILE LOADING

Xiang Liu[1], Dasheng Wei[1], Shengzhe Jin[2], Shun Yang[1],
Dexin Yin[3], Boubou Niakate[3] & David Lasne[3]

[1]School of Energy and Power Engineering, Beihang University, Beijing 100191, China
[2]AVIC Manufacturing Technology Institute, Beijing 100024, China
[3]R&D center and design office, BSS Turbotech Ltd., Beijing 101312, China

Abstract

The high-temperature tensile deformation and damage mechanisms of selective laser melting (SLM)-fabricated Inconel 718 were investigated by combining macroscopic uniaxial tensile testing with in-situ SEM/EBSD characterization at $500\,^{\circ}\mathrm{C}$. Specimens extracted along horizontal and vertical build orientations exhibited comparable yield strengths, while the horizontal specimen showed a slightly higher ultimate tensile strength of 1330 MPa than the vertical specimen of 1280 MPa. The elongation ranged from 6% to 8.5%, and pronounced serrated flow behavior was observed during tensile deformation. The vertical specimen exhibited more frequent B-type serrations, indicating a stronger tendency toward plastic instability. Fractographic observations revealed orientation-dependent fracture characteristics: the horizontal specimen mainly exhibited ductile dimple fracture with limited cleavage facets, whereas the vertical specimen showed river-like patterns, flat fracture regions, and inclusion-associated crack initiation. In-situ tensile observations further revealed the progressive evolution of surface slip traces, lattice rotation, KAM distribution, and GND accumulation. Grain boundaries and twin boundaries affected local slip transmission and deformation compatibility, while second-phase particles and triple junctions promoted local stress concentration, dislocation pile-up, additional slip-system activation, and particle cracking. Local IPF-X analysis further indicated pronounced crystallographic orientation evolution near crack tips and second-phase particles, which was associated with deformation-induced lattice rotation and orientation rearrangement. These results provide direct experimental evidence for understanding grain-scale deformation, strain localization, and damage initiation in additively manufactured Ni-based superalloys under high-temperature tensile loading.

Keywords: Superalloys, Additive Manufacturing, High-temperature Tensile Behavior, Grain Boundary Damage, In-situ Tensile Testing

1. Introduction

Nickel-based superalloys have been widely used in aero-engine and gas-turbine components because of their excellent combination of high-temperature strength, corrosion resistance, oxidation resistance, and microstructural stability. Among them, Inconel 718 (IN718) is one of the most extensively applied precipitation-strengthened Ni-based superalloys, deriving its mechanical strength mainly from the precipitation of γ'' and γ' phases within the face-centered cubic γ matrix. With the increasing demand for geometrically complex and lightweight aerospace components, additive manufacturing (AM), especially selective laser melting (SLM) or laser powder bed fusion (LPBF), has attracted considerable attention for fabricating IN718 components with near-net-shape capability and high material utilization [1, 2].

However, the rapid melting and solidification characteristics inherent to SLM result in microstructures that differ substantially from those produced by conventional wrought or cast processing. Typical SLM-fabricated IN718 exhibits cellular/dendritic substructures, crystallographic texture, residual stress, chemical microsegregation, and processing-induced defects. In particular, Nb segregation during solidification promotes the formation of interdendritic Nb-rich Laves phases and carbides, which can strongly influence the subsequent heat-treatment response and mechanical performance [3–5]. The anisotropic thermal history associated with layer-wise fabrication also leads to orientation-dependent grain structures and mechanical properties, making it necessary to clarify the relationship between build orientation, local microstructure, and high-temperature deformation behavior [5].

For high-temperature applications, the deformation and damage behavior of AM IN718 cannot be fully understood from macroscopic stress–strain curves alone. At intermediate and elevated temperatures, IN718 is prone to serrated flow associated with dynamic strain aging, which originates from interactions between mobile dislocations and diffusing solute atoms [6]. Such plastic instability may enhance strain localization and promote heterogeneous deformation at the grain scale. Meanwhile, microstructural features such as grain boundaries, annealing twin boundaries, pores, inclusions, carbides, and Laves phases can act either as barriers to slip transmission or as preferential sites for strain concentration and crack initiation. In particular, Laves phases have been reported to reduce ductility and toughness and to serve as preferential crack initiation and propagation sites when present in continuous or coarse forms [7].

Grain-scale deformation in polycrystalline superalloys is strongly affected by the compatibility of slip systems across interfaces. Grain boundaries and twin boundaries may either transmit slip or induce dislocation pile-up, depending on the local crystallographic orientation relationship and the active slip systems. These local interactions can produce geometrically necessary dislocation (GND) accumulation, lattice rotation, and strain localization, which eventually contribute to damage initiation. Therefore, direct observation of deformation evolution under load is essential for identifying the microstructural origins of fracture in AM Ni-based superalloys. In-situ tensile testing combined with scanning electron microscopy (SEM) and electron backscatter diffraction (EBSD) provides an effective route to correlate surface slip traces, crystallographic orientation, local misorientation, and GND density during progressive deformation [8].

Although extensive studies have investigated the processing, microstructure, heat treatment, and mechanical properties of SLM-fabricated IN718, the deformation compatibility among grain boundaries, twin boundaries, and second-phase particles under high-temperature tensile loading remains insufficiently understood. In particular, direct evidence linking local slip transfer, GND accumulation, second-phase particle cracking, and final fracture behavior is still limited. Such information is important not only for understanding the failure mechanism of AM IN718, but also for providing experimental support for physics-based constitutive and damage models.

In this study, SLM-fabricated IN718 specimens with different build orientations were investigated under high-temperature tensile loading. Macroscopic uniaxial tensile tests were first conducted to evaluate the orientation-dependent mechanical response and fracture characteristics. Subsequently, in-situ tensile testing at $500\,^{\circ}\mathrm{C}$ was performed in combination with SEM and EBSD characterization to track the evolution of surface slip traces, crystallographic orientation, grain orientation spread (GOS), kernel average misorientation (KAM), and GND density. Special attention was paid to the roles of grain boundaries, annealing twin boundaries, and second-phase particles in deformation compatibility, local strain localization, and damage initiation. The results provide insight into the grain-scale fracture and grain-boundary damage mechanisms of AM Ni-based superalloys under high-temperature tensile loading.

2. Materials and experimental methodology

2.1 Material processing and Specimen fabrication

This study employed the Selective Laser Melting (SLM) process to fabricate the materials. Figure 1 illustrates the preparation workflow of the material blanks: Figure 1a shows the microscopic morphology of the metal powder used in additive manufacturing, Figure 1b presents a schematic illustration

of the SLM process, Figure 1c outlines the printing and specimen sampling strategy, and Figure 1d depicts the heat treatment regime applied to the as-fabricated blanks. Following the extraction of uniaxial tensile round bar specimens, the residual material was utilized to prepare in-situ tensile test specimens. The sampling orientations are illustrated in Figure 2, including the vertical and horizontal directions.

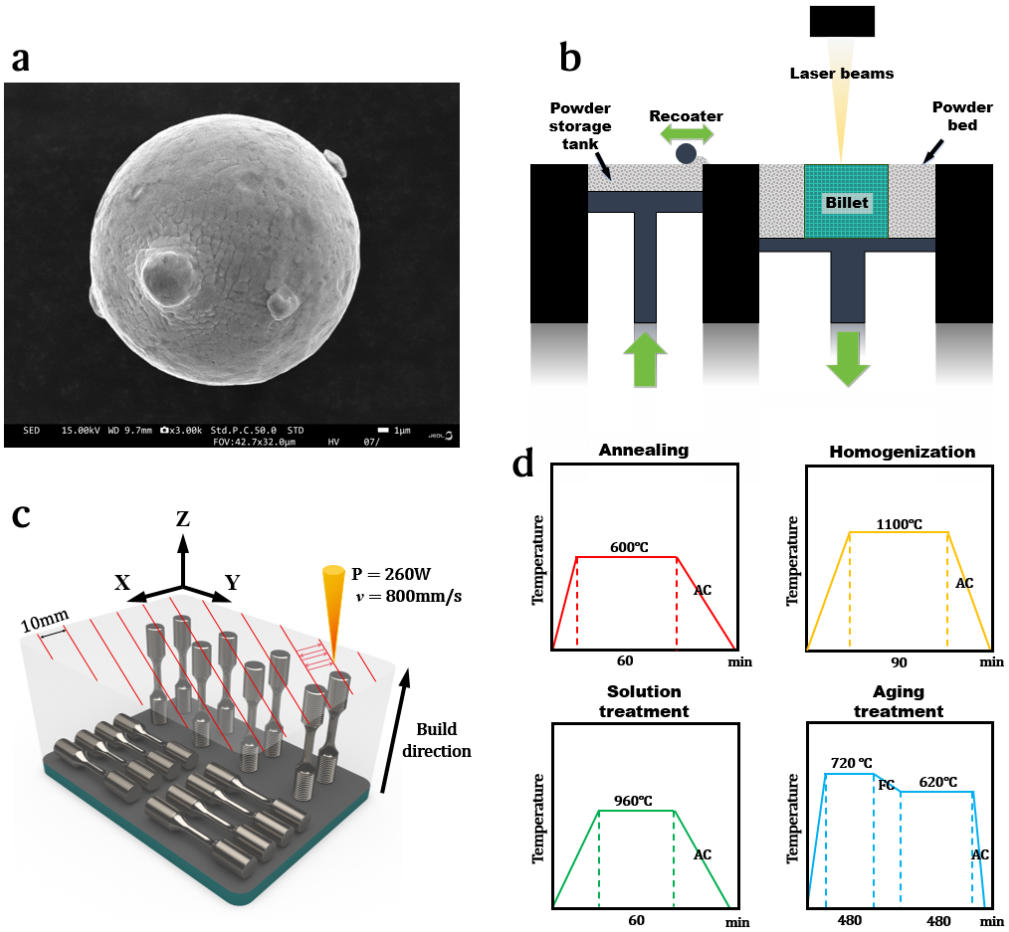


Figure 1 – Schematic illustration of the sample preparation process: (**a**) metal powder; (**b**) schematic illustration of the SLM process; (**c**) printing and sampling strategy; (**d**) heat treatment regime.

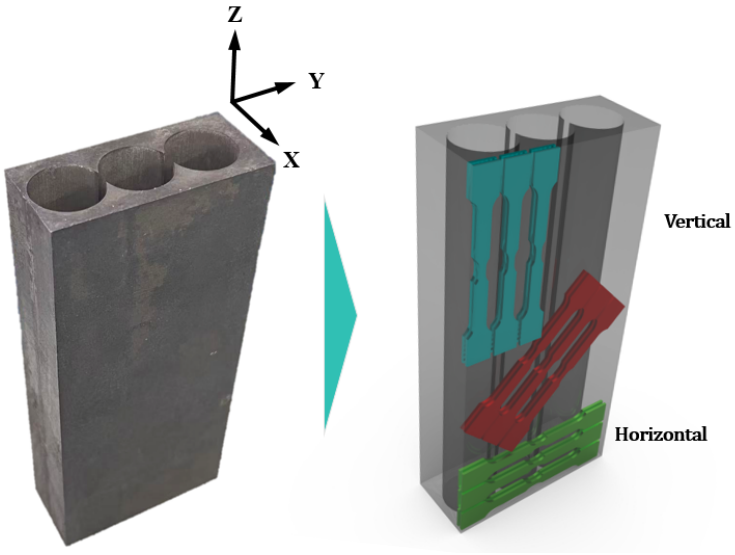


Figure 2 – Schematic illustration of in-situ tensile specimen sampling.

2.2 High-temperature monotonic tensile testing and in-situ tensile testing

Uniaxial tensile tests were performed on a hydraulic servo-controlled testing machine (as shown in Figure 3a). The displacement speed of the crosshead was controlled and maintained at a low loading rate to minimize the influence of strain rate sensitivity. In-situ tensile tests were conducted using an in-situ tensile stage, with specimens securely mounted inside the sample chamber of a scanning electron microscope (SEM) equipped with an EBSD detector via a custom-designed fixture (as shown in Figure 3b).

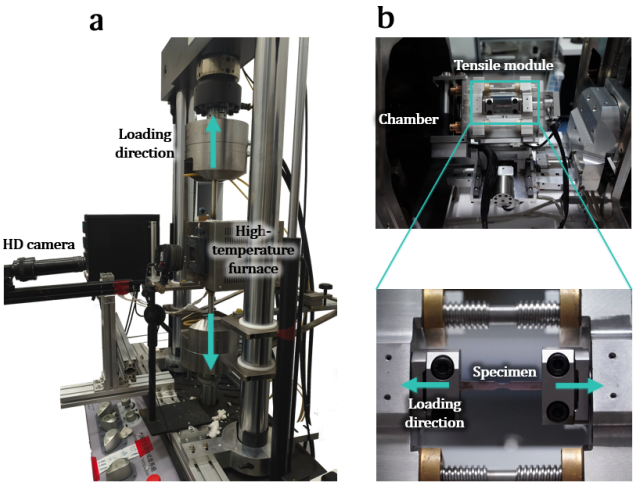


Figure 3 – Schematic illustrations of the test setup for (**a**) uniaxial tensile testing and (**b**) in-situ tensile testing.

3. Results

3.1 Initial microstructure characterization

Figure 4 presents the initial microstructure of two samples with different build orientations. As shown in Figure 4a, the printing strategy leads to distinct crystallographic textures in each orientation, and annealing twins are extensively observed. The KAM maps reveal no significant initial dislocation density on the sample surfaces, indicating low residual strain. The GOS maps show that the material consists predominantly of recrystallized grains, although regions of partially recovered microstructure are still present locally. Figures 4b and 4c display the grain size distribution and misorientation distribution for the two orientations, respectively. Approximately 62% of grain boundaries exhibit a 60° misorientation, consistent with the characteristics of coherent twin boundaries.

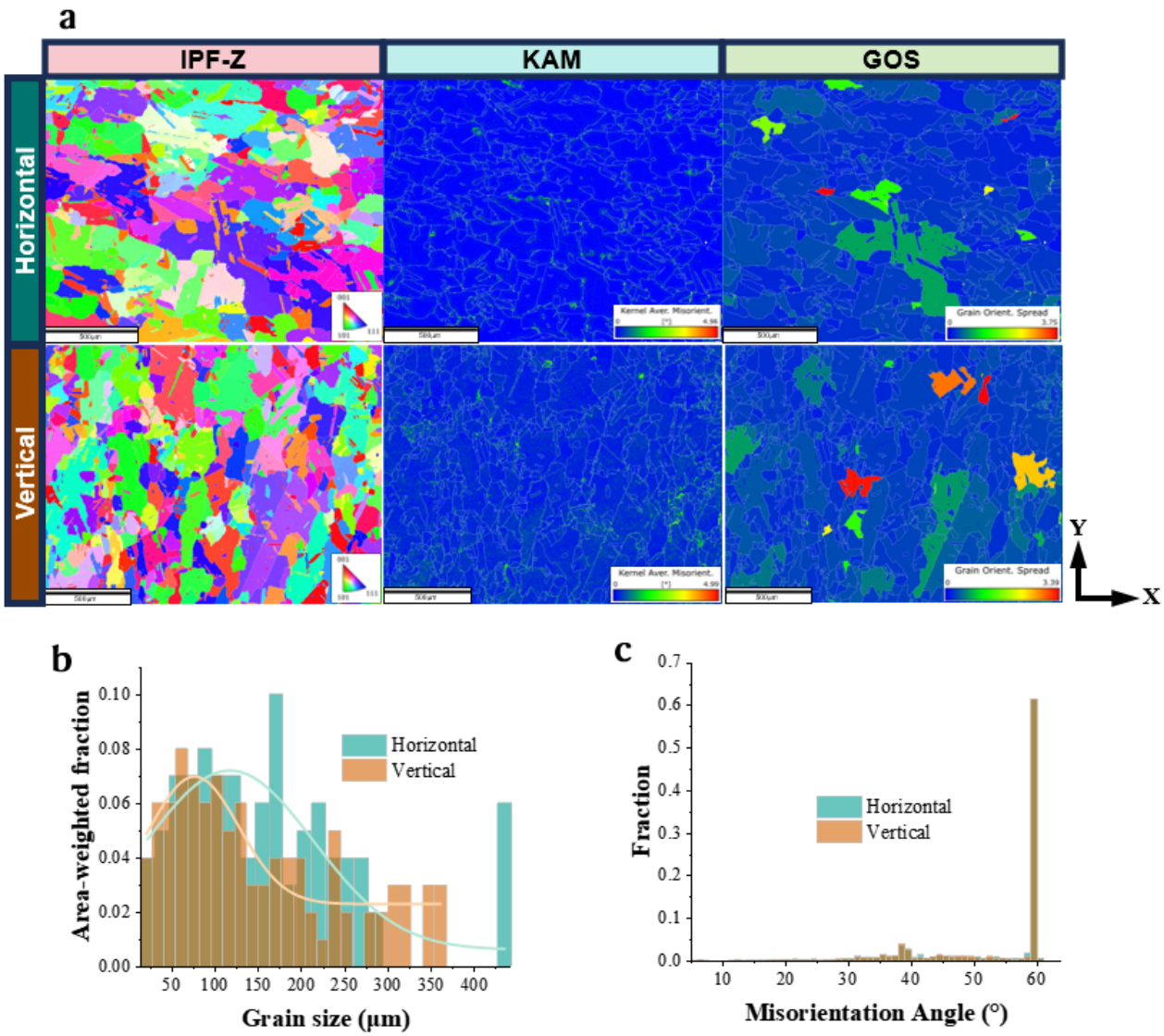


Figure 4 – Initial microstructure morphology of the sample: (**a**) IPF, KAM, and GOS maps for two orientations, (**b**) grain size distribution, and (**c**) grain boundary misorientation distribution.

3.2 Uniaxial tensile test results and fracture surface

Figure 5 presents the uniaxial tensile test results for specimens built along two different orientations. Figure 5b shows a magnified view of the region enclosed by the red box in Figure 1a. The ultimate strength of the Horizontal-direction specimen (1330 MPa) is slightly higher than that of the Vertical-direction specimen (1280 MPa), whereas their yield strengths are comparable. Elongation values exhibit moderate scatter, falling within the range of 6% to 8.5%. Furthermore, as illustrated in Figure 5b, the alloy displays typical serrated flow behavior under the temperature and strain rate conditions employed in this study. Such behavior has been widely reported in additively manufactured nickel-based superalloys [9, 10]. In this work, a combination of B-type and C-type serrations was observed, with B-type serrations occurring more frequently during the tensile deformation of the Vertical-direction specimen, indicating a greater tendency toward plastic instability in this orientation.

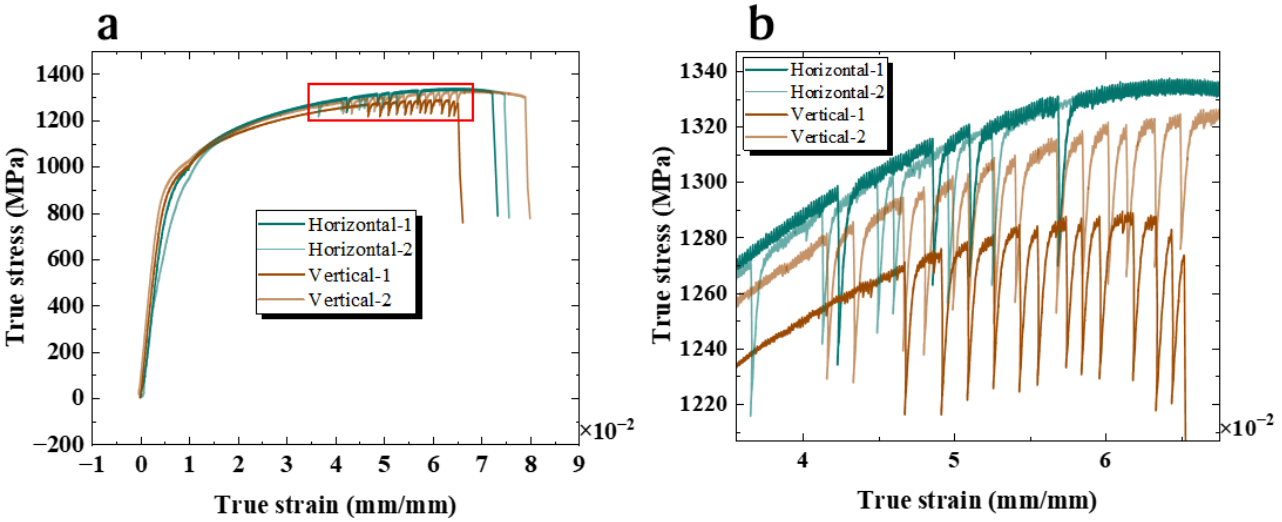


Figure 5 – (**a**) Stress-strain curve of uniaxial tensile specimens; (**b**) Local magnification of the region within the red box in (**a**).

Figure 6 presents SEM observations of the fracture surfaces from the two orientations, where subscripts 1 to 4 denote images at increasing magnifications. As shown in Figure 6a$_1$, the fracture mode of the Horizontal-direction specimen is predominantly ductile, characterized by well-developed dimples (see Figure 6a$_4$), along with a small number of cleavage facets. Clear cleavage planes are observable in Figures 6a$_2$ and 6a$_3$. In contrast, the Vertical-direction specimen exhibits distinct fracture features: river-like patterns are distributed around the nearly parallel fracture surface (Figure 6b$_1$), and inclusion particles are visible on the flat fracture surface (Figure 6b$_2$). A higher-magnification image (Figure 6b$_3$) reveals these morphological details more clearly. Moreover, inclusions of similar size are observed at the root of the dimples, strongly suggesting that these inclusions act as the primary sites for crack initiation.

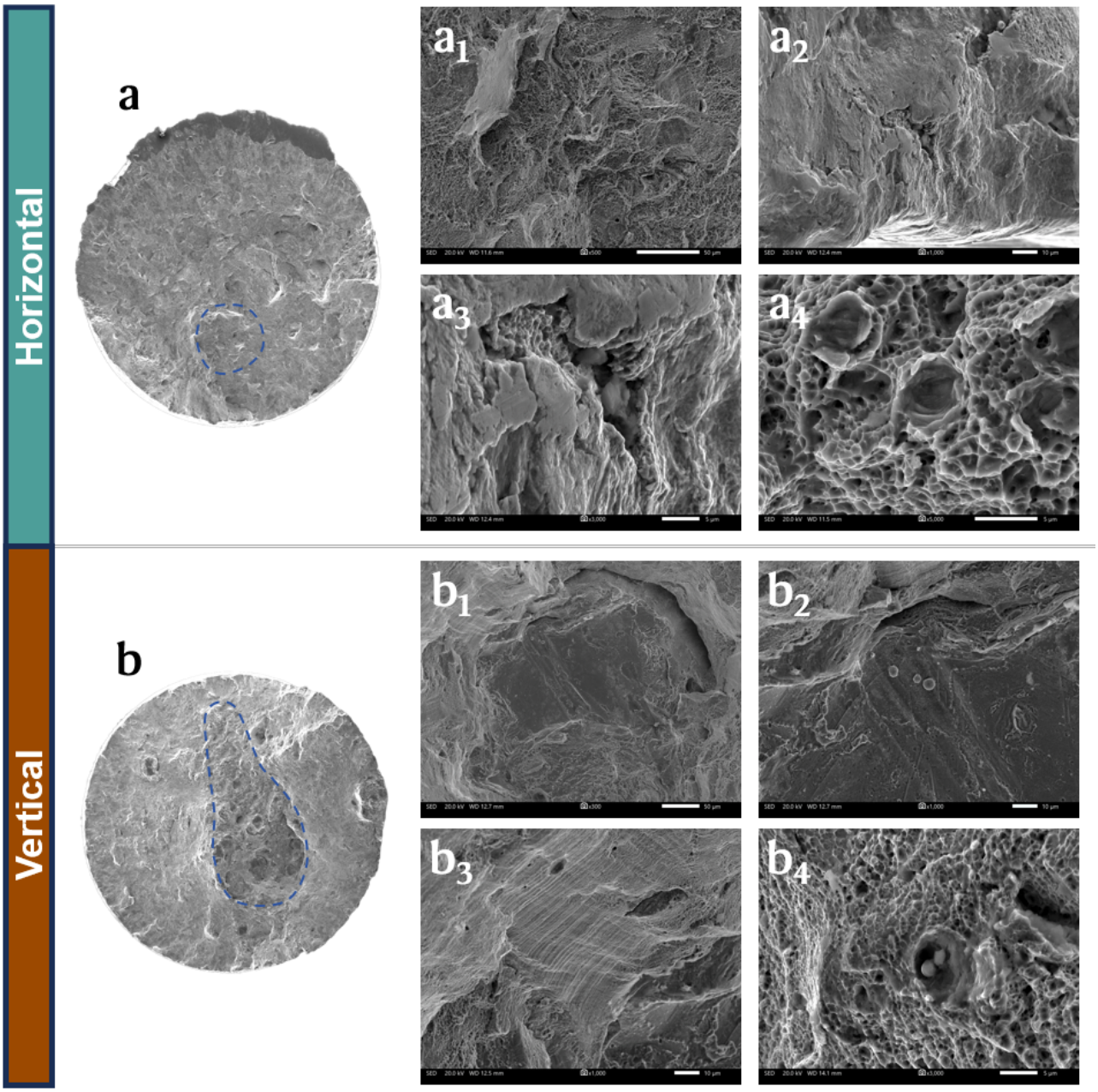


Figure 6 – SEM observation of fracture surfaces in (**a**) horizontal orientation and (**b**) vertical orientation; subscripts 1-4 indicate magnified images at different magnification levels.

3.3 In-situ tensile test results

Figure 7 presents the results of the in situ tensile test of the Horizontal specimen at $500,^{\circ}\mathrm{C}$. In Fig. 7a, six representative moments during the tensile process, denoted as I–VI, were selected for SEM/EBSD characterization. From top to bottom, the images correspond to the surface morphology, inverse pole figure (IPF) orientation map, and kernel average misorientation (KAM) distribution, respectively. Figure 7b shows the corresponding load–displacement curve, in which the six moments marked in Fig. 7a are indicated. These stages are defined as follows: I, initial state; II, yielding point; III/IV, continued loading stages; V, maximum load point; and VI, fracture point.

It can be seen that, with increasing load, the specimen surface gradually evolved from an initially smooth polished state to a distinctly uneven morphology. In the SEM image of the initial state, a small number of circular pores can be observed, as indicated by the white arrows. At the initial state (I), the KAM map shows only a low level of residual strain inside the material, which can be mainly attributed to the release of residual strain by the post-processing annealing treatment. As the load increased and the specimen reached the yielding stage (II), obvious slip traces appeared on the surface, accompanied by pronounced local surface undulations caused by lattice rotation. At this stage, no significant dislocation accumulation was observed inside the relatively large grains. Instead, dislocations were mainly concentrated in small grains between larger grains, near grain boundaries, and around twin boundaries.

With further loading (III and IV), the surface roughening became more pronounced, and the dislocation accumulation reflected by the KAM distribution increased significantly. When the load reached stage IV, slip had occurred in almost all grains except for a few isolated ones. In addition, obvious intragranular orientation changes were observed in some grains, such as the region marked by the black arrow in Fig. 7a-IV. At the maximum load point (V), the dislocation density reached its peak and was mainly concentrated in regions containing fine grains. At the final fracture stage (VI), the orientations of most grains had changed considerably, and pronounced dislocation concentration near grain boundaries could be clearly observed, as indicated by the dark red arrows.

To further quantitatively analyze the evolution of local strain at different loading stages, the KAM count distributions of each stage were extracted and plotted in Fig. 7c. Theoretically, since each image contains the same number of pixels, the area under each KAM count curve should remain identical. Both the peak intensity and peak position changed significantly with increasing load. In the initial state (I), the KAM count distribution was relatively concentrated, and the peak corresponded to a low KAM value, indicating that the material was in a relatively uniform low-residual-strain state. As the load continued to increase, the peak of the KAM count distribution gradually decreased, while the peak position shifted toward higher KAM values. This indicates that the overall strain level increased, while the internal strain distribution gradually evolved from a uniform state to a more heterogeneous and localized state.

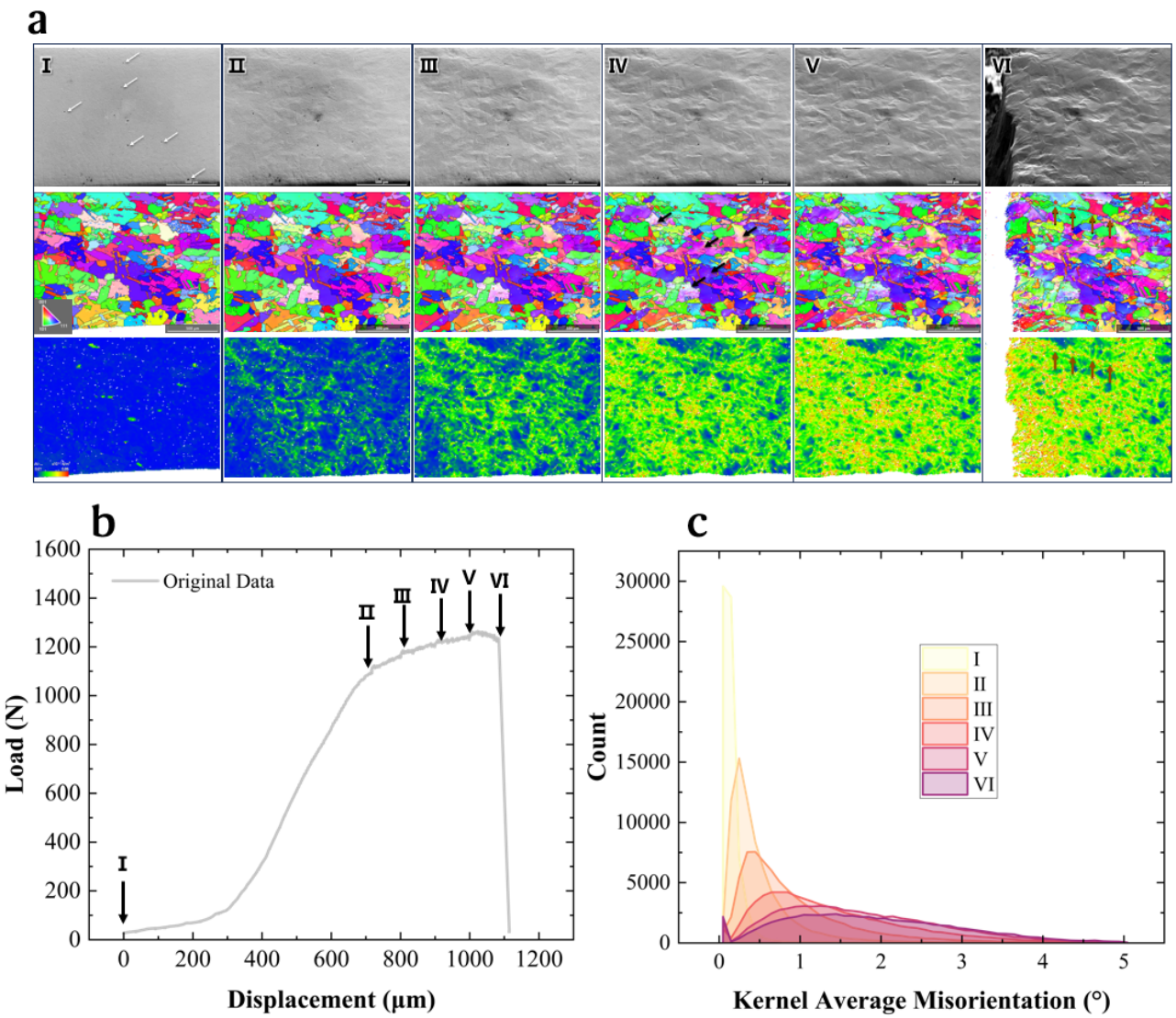


Figure 7 – In-situ tensile test results for the horizontal specimen at 500℃: (**a**) SEM/EBSD images at different stages of the tensile process (I-VI); (**b**) load-displacement curve with corresponding stages marked; (**c**) KAM count distribution at each stage.

4. Discussion

Figure 8 presents enlarged observations of selected regions at different loading stages. Specifically, Figure 8a–d correspond to loading stages II–V in Figure 7, respectively, while the subscripts 1–4 denote the SEM surface morphology, IPF map, GOS map, and GND density map, respectively. The GND density was estimated based on the method proposed by Kubin and Mortensen [11], as expressed by

$$\rho_{\mathrm{GND}} = \frac{\alpha\theta}{db} \tag{1}$$

where α is a constant related to the boundary type. For a pure tilt boundary, $\alpha = 2$, whereas for a pure twist boundary, $\alpha = 4$ [12]. θ is the local misorientation angle, which is commonly characterized by KAM; d is the EBSD step size; and b is the magnitude of the Burgers vector. In this study, α was taken as 3, b was taken as the magnitude of the $0.5\langle 110\rangle$-type Burgers vector, and the EBSD step size d was $0.12\ \mu\mathrm{m}$. It should be noted that the legends or color scales for all types of images in Figure 8 are only shown in Figure 8a, and the subsequent images, namely Figure 8b–d, use the same legend and color-scale settings.

At the yield-point load, pronounced slip traces were observed on the specimen surface. Over most regions of this grain boundary, no significant barrier effect against slip transmission was observed. As a result, the slip traces formed in G1 could continuously extend into G2, thereby promoting coordinated deformation between the two grains, as indicated by the black arrows in Figure 8a1. This phenomenon is also supported by the GOS distribution in Figure 8a$_3$, where no pronounced strain localization can be observed within the corresponding grains at this stage. The GND distribution further indicates that the dislocation distribution inside the grains remains relatively uniform.

However, it is worth noting that a distinct region of dislocation accumulation appears at the boundary between G1 and G2, as marked by the red circle in Figure 8a$_4$. Combined with the surface morphology shown in Figure 8a$_1$, it can be inferred that the dislocation pile-up in this region may be associated with a small second-phase particle. This particle induces local deformation incompatibility and stress concentration, thereby activating another slip system in G2, as indicated by the yellow arrow. Meanwhile, a slip band composed of dense slip traces can be observed near the circled region, further suggesting locally intensified plastic deformation at this site.

As the load further increased, similar deformation mechanisms were also observed in other regions. As shown in Figure 8b$_1$, G3 and G3′ form a twin pair, with G3′ being a typical annealing twin. Based on the orientations of the surface slip traces, the possible intersections between the active slip planes and the specimen surface were drawn in Figure 8b$_1$. Slip traces with similar inclination angles were marked using the same color. In addition, two red circles were used to mark a suspected Nb-rich second-phase particle located at the grain boundary and a triple-junction region, respectively.

The suspected second-phase particle is located near the junction of G3, G3′, and G4, and exhibits obvious cracking. The orientation of its fracture surface is close to that of the major slip traces in G4, as indicated by the cyan arrow, suggesting that the cracking of this particle may originate from local deformation incompatibility induced when dislocation slip within the matrix is transmitted to the surface. Due to the difference in plastic deformability between the second-phase particle and the matrix, stress concentration is prone to develop around the particle, eventually leading to cracking of the brittle second-phase particle.

Similar to the phenomenon observed in Figure 8a$_1$, another slip system was activated near the second-phase particle in addition to the primary slip system in G4, as indicated by the yellow arrow, whereas the primary slip traces are marked by the cyan arrow. Considering the crystallographic orientations of G2 and G4, together with the consistency of the observed phenomena in these two regions, it is reasonable to conclude that such second-phase particles play an important role in triggering the activation of additional slip systems. Further evidence for this interpretation will be provided by another observation discussed below.

In addition, because the second-phase particles and the triple-junction region impose strong constraints on local plastic deformation, pronounced GND accumulation appears at these locations, as marked by the three red circles in Figure 8c$_4$. However, the dislocation pile-up caused solely by the grain boundary does not activate an additional slip system, indicating that the second-phase particle

is more likely to be the key factor responsible for this phenomenon than an ordinary grain boundary. The low-magnification image in Figure 8c_1 provides further evidence supporting this mechanism. In Figure 8c_3, four relatively large second-phase particles are marked by red circles. These particles induce additional slip activity in both G4 and G7, which have similar crystallographic orientations, further demonstrating that second-phase particles play an important role in local slip-system activation and strain localization.

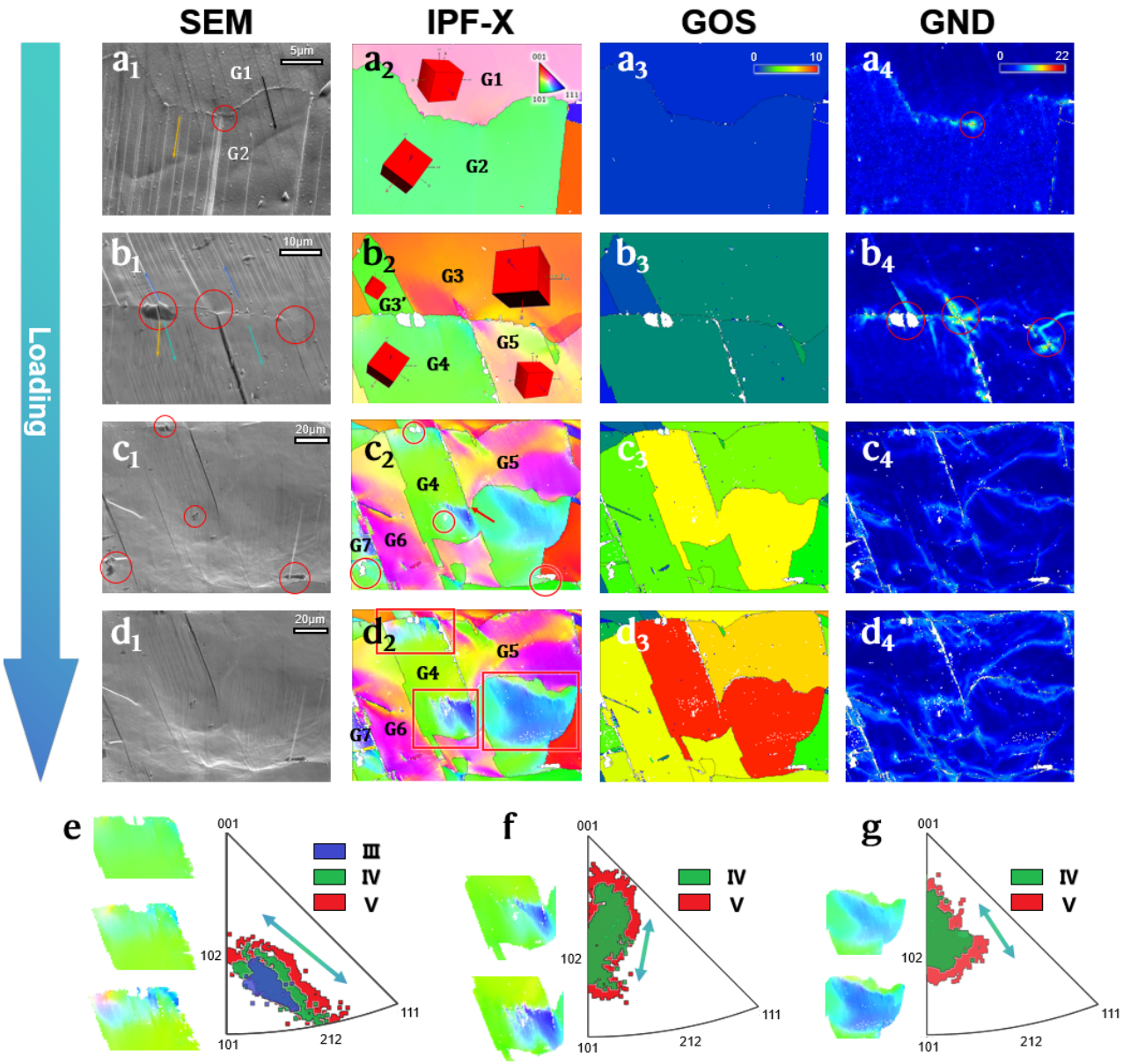


Figure 8 – Local deformation and crystallographic orientation evolution associated with grain boundaries, twin boundaries, and second-phase particles during in-situ tensile loading. (**a-d**) Enlarged SEM/EBSD observations at loading stages II–V in Figure 7, respectively. The subscripts 1–4 denote SEM surface morphology, IPF map, GOS map, and GND density map, respectively. (**e-g**) Local IPF-X orientation distributions extracted from the representative regions marked in (**d2**), where X denotes the tensile direction.

Another phenomenon worthy of attention is the local crystallographic orientation evolution during tensile deformation. To further analyze this phenomenon, three representative regions within grain G4 were selected, as marked by the red rectangles in Fig. 8d2. The IPF-X orientation features of these regions were then extracted, where X denotes the tensile direction, and the corresponding local IPF-X distributions at different loading stages are presented in Figs. 8e–g.

As shown in Fig. 8b2, the initial orientation of G4 is likely close to the $\langle -230 \rangle$ direction, as indicated by the blue scatter points in Fig. 8e. During tensile deformation, under the combined influence of the second-phase particle located at the junction of G3, G3′, and G4, the G3/G4/G5 triple junction, and the G4/G6 twin boundary, the orientation distribution in this region gradually evolves toward the $\langle 102 \rangle$ and $\langle 212 \rangle$ directions.

For the region shown in Fig. 8f, the grain boundary between G4 and G5 has cracked to a certain extent during deformation. Therefore, the region indicated by the red arrow in Fig. 8c2 can be approximately regarded as a crack tip, which acts as a dislocation emission source, as shown in Figs. 8c4 and 8d4. Consequently, a considerable fraction of the orientation distribution in Fig. 8f is already concentrated near the $\langle 102 \rangle$ direction at an earlier stage, as indicated by the green scatter points in Fig. 8f. With further tensile deformation, under the combined effects of the crack tip and the second-phase particle, the local orientation further evolves toward the $\langle 001 \rangle$ direction, as shown by the red scatter points in Fig. 8f.

For the region shown in Fig. 8g, the orientation evolution is not significantly affected by any specific microstructural feature. Instead, the orientation distribution gradually spreads outward from the $\langle 102 \rangle$ direction. This indicates that, in regions without strong local constraints or pronounced stress concentration sources, the crystallographic orientation evolves in a relatively gradual manner.

In summary, second-phase particles, grain boundaries, and twin boundaries play important roles in local deformation compatibility, stress concentration, dislocation accumulation, and slip-system activation, eventually leading to local strain concentration and damage initiation. In addition, under the combined influence of these microstructural features, pronounced local crystallographic orientation evolution occurs during tensile deformation. This phenomenon is more likely associated with deformation-induced lattice rotation and orientation rearrangement, and its underlying mechanism requires further investigation through phase identification and higher-resolution characterization in future studies.

5. Contact Author Email Address

Mailto: yangshun_academic@buaa.edu.cn

6. Copyright Statement

The authors confirm that they, and/or their company or organization, hold copyright on all of the original material included in this paper. The authors also confirm that they have obtained permission, from the copyright holder of any third party material included in this paper, to publish it as part of their paper. The authors confirm that they give permission, or have obtained permission from the copyright holder of this paper, for the publication and distribution of this paper as part of the ICAS proceedings or as individual off-prints from the proceedings.

References

[1] Xiaoqing Wang, Xibing Gong, and Kevin Chou. Review on powder-bed laser additive manufacturing of inconel 718 parts. *Proceedings of the Institution of Mechanical Engineers, Part B: Journal of Engineering Manufacture*, 231(11):1890–1903, 2017.

[2] K. N. Amato, S. M. Gaytan, L. E. Murr, E. Martinez, P. W. Shindo, J. Hernandez, S. Collins, and F. Medina. Microstructures and mechanical behavior of inconel 718 fabricated by selective laser melting. *Acta Materialia*, 60(5):2229–2239, 2012.

[3] G. A. Knorovsky, M. J. Cieslak, T. J. Headley, A. D. Romig, and W. F. Hammetter. Inconel 718: A solidification diagram. *Metallurgical Transactions A*, 20:2149–2158, 1989.

[4] Edward Chlebus, Konrad Gruber, Bogumiła Ku'znicka, Tomasz Kurzynowski, and Jerzy Kurzac. Effect of heat treatment on microstructure and mechanical properties of inconel 718 processed by selective laser melting. *Materials Science and Engineering: A*, 639:647–655, 2015.

[5] Dunyong Deng, Ru Lin Peng, Håkan Brodin, and Johan Moverare. Microstructure and mechanical properties of inconel 718 produced by selective laser melting: Sample orientation dependence and effects of post heat treatments. *Materials Science and Engineering: A*, 713:294–306, 2018.

[6] Sachin Nalawade, Sundararaman Mahadevan, Jung Bahadur Singh, Kishore Ramaswamy, and Amit Verma. Serrated yielding in alloy 718. In *Superalloys 2010*, pages 809–823. The Minerals, Metals & Materials Society, 2010.

[7] John J. Schirra, Robert H. Caless, and Robert W. Hatala. The effect of laves phase on the mechanical properties of wrought and cast + hip inconel 718. In Edward A. Loria, editor, *Superalloys 718, 625 and Various Derivatives*, pages 375–388. The Minerals, Metals & Materials Society, 1991.

[8] Jalal Al-Lami, Thibaut Dessolier, Talha Pirzada, and Minh-Son Pham. Dislocation distribution, crystallographic texture evolution and plastic inhomogeneity of inconel 718 fabricated by laser powder-bed fusion, 2023.

[9] Yu Qin, P. Alex Greaney, T. Matthew Evans, and Jamie J. Kruzic. A critical dislocation velocity for serration mechanism transition in a nickel-chromium solid solution alloy. *International Journal of Plasticity*, 145:103071, October 2021.

[10] Xiang Liu, Dasheng Wei, Shun Yang, Dexin Yin, Xinlei Yan, Yaoyao Ding, and Boubou Niakate. Uniaxial and cyclic deformation behavior of selective laser melted GH4169 superalloy at elevated temperature: Insights into Portevin–Le Chatelier effect and strain-amplitude softening. *Materials Science and Engineering: A*, 953:149661, February 2026.

[11] L.P Kubin and A Mortensen. Geometrically necessary dislocations and strain-gradient plasticity: a few critical issues. *Scripta Materialia*, 48(2):119–125, January 2003.

[12] Q. Liu, D. Juul Jensen, and N. Hansen. Effect of grain orientation on deformation structure in cold-rolled polycrystalline aluminium. *Acta Materialia*, 46(16):5819–5838, October 1998.